$Eu_3Ir_2In_{15}$: A Mixed-Valent and Vacancy-Filled Variant of the $Sc_5Co_4Si_{10}$ Structure Type with Anomalous Magnetic Properties

Sumanta Sarkar,[†] Swastika Banerjee,[†] Rajkumar Jana,[†] Ramesh Siva,[†] Swapan K. Pati,[†,‡] Mahalingam Balasubramanian,[§] and Sebastian C. Peter[*,†]

[†]New Chemistry Unit and [‡]Theoretical Science Unit, Jawaharlal Nehru Centre for Advanced Scientific Research, Jakkur, Bangalore, 560064, India

[§]Advanced Photon Source, Argonne National Laboratory, Argonne, Illinois 60439, United States

S *Supporting Information*

ABSTRACT: A new compound, $Eu_3Ir_2In_{15}$, has been synthesized using indium as an active metal flux. The compound crystallizes in the tetragonal $P4/mbm$ space group with lattice parameters $a = 14.8580(4)$ Å, $b = 14.8580(4)$ Å, and $c = 4.3901(2)$ Å. It was further characterized by SEM-EDX studies. The effective magnetic moment (μ_{eff}) of this compound is 7.35 μ_B/Eu ion with a paramagnetic Curie temperature (θ_p) of −28 K, suggesting antiferromagnetic interaction. The mixed-valent nature of Eu observed in magnetic measurements was confirmed by XANES measurements. The compound undergoes demagnetization at a low magnetic field (10 Oe), which is quite unusual for Eu-based intermetallic compounds. Temperature-dependent resistivity studies reveal that the compound is metallic in nature. A comparative study was made between $Eu_3Ir_2In_{15}$ and hypothetical vacancy-variant $Eu_5Ir_4In_{10}$, which also crystallizes in the same crystal structure. However, our computational studies along with control experiments suggest that the latter is thermodynamically less feasible compared to the former, and hence we propose that it is highly unlikely that an $RE_5T_4X_{10}$ would exist with X as a group 13 element.
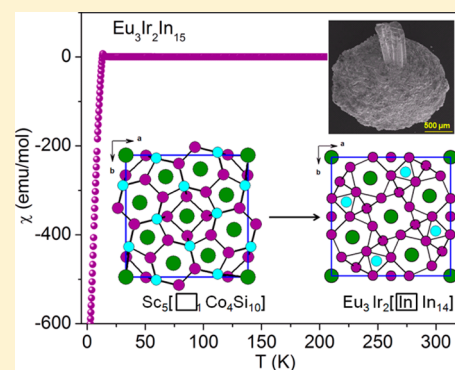
1. INTRODUCTION

Recent developments in superconductivity, thermoelectric devices, topological insulators, and materials with giant magnetoresistance have revoked the enthusiasm of both chemists and materials scientists to explore new Zintl phases, which were first studied by Eduard Zintl. The recent examples are $Ba_2Sn_3Sb_6$ and $SrSn_3Sb_4$, which show superconductivity below 3.9 K,[1] $Yb_{14}MnSb_{11}$ and its substituted variants are one of the most studied Zintl phases for their thermoelectric applications,[2−7] Sr_2X (X = Pb, Sn) undergo a stress-driven nontrivial topological state,[8] and $Eu_3Ga_2P_4$ shows giant magnetoresistance.[9] These compounds generally contain one or more of the electropositive alkali or alkaline earth metals and p-block elements. Indium-based Zintl phases, commonly known as "polyindides", are one of the most studied families of intermetallic compounds owing to their diverse structural features, bonding, and interesting physical properties. A general structural feature in this class of compounds is distorted body-centered-like indium cubes, which are also found in the structure of elemental indium. These units can be used as building blocks to construct different structures using different binding strategies; for example, in our previous work we showed how RET_2In_4 (RE = rare earths; T = transition metal) that have complex three-dimensional (3D) T_2In_4 polyanionic networks could be obtained from simple $REIn_2$ structures that are basically derived from an AlB_2 structure type.[10] There is a plethora of indium-based Zintl phases reported in the literature

studied for their structure−property relationship, and they can broadly be divided into two classes: the first one contains main group elements, mainly alkali, alkaline earth, and rare earth metals, e.g., MIn_2 (M = Ca, Sr, Ba, rare earths),[11] Sr_3In_5, $SrIn_4$, and Sr_3In_{11}.[12] The second class of compounds contains additional transition metals, which inevitably give rise to more complex structure and bonding characteristics. In the latter class, the structural as well as bonding features are dictated by the relative ratios of transition metal and indium. Consequently, they were further classified into three subclasses by Kalychak et al.[13] The first class of compounds with high transition metal content has complex multilayer structures with high values for the coordination numbers (CN) of all atom types. The second category of compounds is in the region with higher rare earth content. The shortest lattice parameter in these compounds ranges from ∼360 to 420 pm and consists of two layers of atoms. The third group of compounds contains the highest rare earth content among all three classes and mostly has complex multilayer structures, with the value of the shortest lattice parameter of 9 Å or more. A common structural motif of these kinds of systems is the occurrence of body-centered indium cubes. Heavier and more electronegative d^{10} or $d^{10}s^1$ transition metals (T) increase the polarity in the networks, bringing additional stabilization and distortion in the

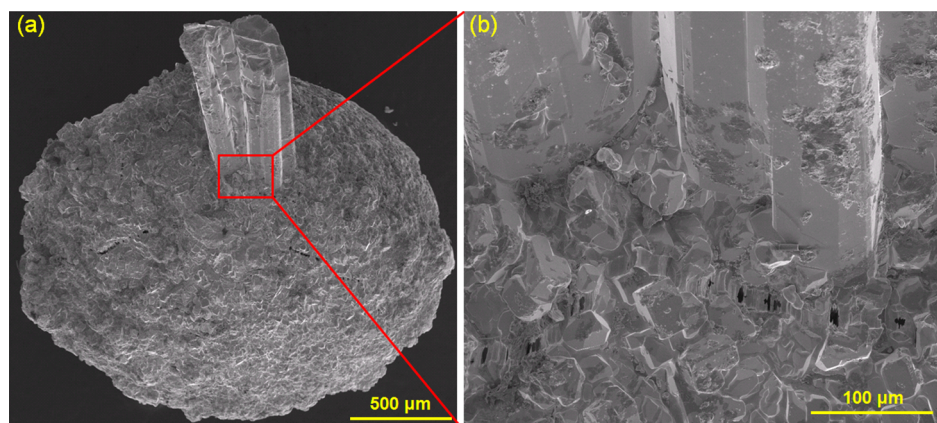**Figure 1.** (a) FE SEM image of a representative single crystal of $Eu_3Ir_2In_{15}$ protruding from a silicon globule. (b) Enlarged image of the crystal growth site where small crystallites are visible.

indium cubes. While the stronger heteroatomic $T-X$ bonds replace the weaker homoatomic $X-X$ bonds, especially for the third row of T, there is noticeable enhancement in the flexibility and variety of condensation modes of polyanionic networks. In many polyindides, the indium content in the system is exceedingly high; for example, Lei et al.[12] first reported a new intermetallic compound, $Eu_3Co_2In_{15}$, with its own structure type along with another Zintl phase, K_2CoIn_9. Although the electronic structure was studied in detail, little attention was paid towards the crystal structure and physical properties of the compound. This motivated us to investigate analogous compounds with the other two group members of cobalt.

In this report, we present a detailed account on the structure−property relationship of $Eu_3Ir_2In_{15}$. Two successive magnetic transitions were observed in this compound followed by a strange demagnetization leading to negative magnetic susceptibility. During the systematic structural analysis of this compound by single-crystal X-ray diffraction, we came across a striking similarity with the crystal structure of $RE_5T_4X_{10}$ (X = p-block metals) family compounds.[14−17] Both crystallize in the tetragonal $P4/mbm$ space group, with the latter having a vacancy in one of the p-block sites. A further investigation in the literature revealed an astonishing trend: so far all the compounds reported in $RE_5T_4X_{10}$ contain solely group 14 metals (Si, Ge, Sn), with no report of any compound with group 13 metals in this class. In contrast, there is no report with group 14 forming an $RE_3T_2X_{15}$ composition. This motivated us to study the feasibility of formation as well as stability of these compounds in terms of the chemical potentials of individual atomic sites present in each of these compounds, and we found out that the coordination environment around each site plays a crucial role toward the overall stability of the compound by dispersing the electron densities throughout the crystal structure. $Eu_3Ir_2In_{15}$ gains more stability on these grounds over the hypothetically predicted $Eu_5Ir_4In_{10}$.

2. EXPERIMENTAL SECTION

2.1. Synthesis. *2.1.1. Chemicals Used.* Europium (ingots, 99.99%, ESPI metals), iridium (powder, 99.99%, Alfa Aesar), silicon (granular, 99.999%, 0.25 in. or less, Alfa Aesar), and indium (tear drops, 99.99%, Alfa Aesar) were used as purchased without any further purification.

2.1.2. Metal Flux Method. A 3 mmol amount of europium, 2 mmol of iridium, 6 mmol of Si, and 30 mmol of indium were taken in an alumina crucible under an inert (argon) atmosphere inside a glovebox

(H_2O, O_2 levels <0.1 ppm). The purpose of excess indium is to act as an active metal flux, and that of silicon to nucleate the crystal growth. The crucible was placed in a 13 mm quartz tube and flame-sealed under a vacuum of 10^{-4} Torr, to prevent oxidation during heating. The tube was then placed in a vertical tube furnace, heated to 1273 K in 10 h, and kept at that temperature for 6 h. The temperature was then lowered to 1123 K in 2 h and annealed at this temperature for 72 h. Finally, the system was allowed to cool slowly to room temperature in 48 h. The reaction products were isolated from the excess indium flux by heating at 623 K and subsequent centrifugation through a coarse frit. The remaining flux was removed by immersion and sonication in glacial acetic acid for 24 h. The final crystalline products were rinsed with water and dried with acetone in a vacuum oven at 350 K for 12 h. The $Eu_3Ir_2In_{15}$ compound was grown as shiny thin rod-shaped crystals with an average length of 4−5 mm and was insensitive to air and moisture with no decomposition observed even after several months. Attempts to synthesize bulk compounds by high-frequency induction heating were unsuccessful.

2.1.2. Direct Heating. Metallic pieces of europium, iridium, and indium were taken in the stoichiometric ratio of 3:2:15, respectively, in a tantalum ampule and sealed in an evacuated quartz tube. The same temperature profile was used for the direct heating synthesis as in the metal flux method. The brittle product with metallic luster was separated from the tantalum tube. No side reaction with the container was observed. The compound was stable in ambient conditions for at least several months. The products were obtained in high yield (>95%), and no other impurity phases were found except some extraneous indium metal, as confirmed from the powder X-ray diffraction (Figure S1).

2.2. Elemental Analysis. Quantitative microanalysis on $Eu_3Ir_2In_{15}$ was performed with a FEI NOVA NANOSEM 600 instrument equipped with an EDAX instrument. Data were acquired with an accelerating voltage of 20 kV and a 100 s accumulation time. A typical metallic rod-shaped single crystal of $Eu_3Ir_2In_{15}$ obtained from the metal flux method is shown in Figure 1. The EDX analysis was performed using the P/B-ZAF standardless method (where Z = atomic no. correction factor, A = absorption correction factor, F = fluorescence factor, P/B = peak to background model) on visibly clean surfaces of the crystals. The microanalysis on different spots on the crystal gave an average molar composition in good agreement with the composition obtained from the single-crystal XRD refinement (Figure S2).

2.3. Single-Crystal X-ray Diffraction. A crystal of suitable size (0.28 × 0.10 × 0.04 mm^3) was cut from a rod-shaped crystal and mounted on a thin glass (∼0.1 mm) fiber with commercially available superglue. X-ray single-crystal structural data for $Eu_3Ir_2In_{15}$ were collected at room temperature as well as at 100 K on a Bruker Smart Apex 2 CCD diffractometer. A normal-focus, 2.4 kW sealed tube X-ray source with graphite monochromatic Mo Kα radiation (λ = 0.710 73 Å) operating at 50 kV and 30 mA was used in the ω-scan mode. The

data were collected using a full sphere of 60 frames acquired up to 73.28° in 2θ. The individual frames were measured with steps of 0.50° and an exposure time of 30 s per frame. The program SAINT[18] was used for integration of diffraction profiles along with the SADABS package suite[19] to apply numerical absorption corrections.

2.4. Structure Refinement. The preliminary data collection was performed at shorter exposure time (10 s, 20 s), but it did not yield any convincing refinement probably due to high X-ray absorption by the compound. However, initial indexing suggested a primitive tetragonal crystal system and $4/mmm$ Laue class with lattice parameters a = 14.8580(4) Å, b = 14.8580(4) Å, and c = 4.3901(2) Å, the refinement reached convergence, and the residual parameters became well behaved. Lattice symmetry and parameters were found to be compatible with both $Sc_5Co_4Si_{10}$ and $Eu_3Co_2In_{15}$ structure types. We started the refinement by taking the atomic coordinates of $Sc_5Co_4Si_{10}$ as a model, and the structures were refined using SHELXL-97 (full-matrix least-squares on F^2)[20] with anisotropic atomic displacement parameters for all atoms. However, the starting residual (R_1) and electron density maps were very high, 76% and 186 and -203 e A^{-3}, respectively, indicating the model might not be correct. Hence we used the atomic coordinates of $Eu_3Co_2In_{15}$ and repeated the refinement process. The occupancy parameters were refined in a separate series of least-squares cycles in order to check the correct composition. The initial statistical parameters were well behaved and converged well. The final compositions of the compound obtained from single-crystal XRD data corroborated well with EDX data. The data collection and refinement parameters of $Eu_3Ir_2In_{15}$ are summarized in Table 1. The atomic coordinates and equivalent atomic displacement parameters, anisotropic atomic displacement parameters, and important bond lengths are listed in Tables 2, 3, and 4, respectively.

Table 1. Crystal Data and Structure Refinement for $Eu_3Ir_2In_{15}$ at 100(2) K

empirical formula	$Eu_3Ir_2In_{15}$
fw	2562.58
wavelength	0.71073 Å
cryst syst	tetragonal
space group	$P4/mbm$
unit cell dimens	a = 14.8186(14) Å
	b = 14.8186(14) Å
	c = 4.3742(4) Å
volume	960.53(16) Å^3
Z	2
density (calcd)	8.860 g/cm^3
absorp coeff	40.988 mm^{-1}
F(000)	2156
cryst size	0.28 × 0.10 × 0.04 mm^3
θ range for data collection	2.75° to 25.99°
index ranges	$-14 \leq h \leq 18$, $-12 \leq k \leq 18$, $-5 \leq l \leq 5$
reflns collected	3387
indep reflns	561 [R_{int} = 0.0514]
completeness to θ = 25.99°	98.6%
refinement method	full-matrix least-squares on F^2
data/restraints/params	561/48/37
goodness-of-fit	1.320
final R indices [>2σ(I)][a]	R_{obs} = 0.0636
	wR_{obs} = 0.1856
R indices [all data][a]	R_{all} = 0.0639
	wR_{all} = 0.1857
extinction coeff	0.00047(3)
largest diff peak and hole	5.687 and -3.462 e Å^{-3}

$^aR = \sum||F_o| - |F_c||/\sum|F_o|$, $wR = \{\sum[w(|F_o|^2 - |F_c|^2)^2]/\sum[w(|F_o|^4)]\}^{1/2}$ and calc $w = 1/[\sigma^2(F_o^2) + (0.0620P)^2 + 408.3495P]$ where $P = (F_o^2 + 2F_c^2)/3$.

Table 2. Atomic Coordinates ($\times 10^4$) and Equivalent Isotropic Displacement Parameters ($Å^2 \times 10^3$) for $Eu_3Ir_2In_{15}$ at 100(2) K with Estimated Standard Deviations in Parentheses

label	x	y	z	occupancy	U_{eq}[a]
Eu(1)	0	0	5000	1	2(1)
Eu(2)	3249(1)	1751(1)	5000	1	3(1)
Ir	1230(1)	3770(1)	5000	1	3(1)
In(1)	0	5000	5000	1	5(1)
In(2)	2068(1)	2932(1)	0	1	2(1)
In(3)	681(1)	2051(1)	5000	1	5(1)
In(4)	1526(1)	4985(1)	0	1	1(1)
In(5)	1568(1)	824(1)	0	1	3(1)

$^aU_{eq}$ is defined as one-third of the trace of the orthogonalized U_{ij} tensor.

Table 3. Anisotropic Displacement Parameters ($Å^2 \times 10^3$) for $Eu_3Ir_2In_{15}$ at 100(2) K with Estimated Standard Deviations in Parentheses^a

label	U_{11}	U_{22}	U_{33}	U_{12}	U_{13}	U_{23}
Eu(1)	2(1)	2(1)	2(1)	0	0	0
Eu(2)	3(1)	3(1)	3(1)	1(1)	0	0
Ir	3(1)	3(1)	1(1)	0(1)	0	0
In(1)	5(1)	5(1)	4(1)	0(1)	0	0
In(2)	2(1)	2(1)	2(1)	0(1)	0	0
In(3)	5(1)	4(1)	4(1)	0(1)	0	0
In(4)	1(1)	1(1)	2(1)	0(1)	0	0
In(5)	3(1)	3(1)	4(1)	0(1)	0	0

^{a}The anisotropic displacement factor exponent takes the form $-2\pi^2[h^2a^{*2}U_{11} + ... + 2hka^*b^*U_{12}]$.

Table 4. Bond Lengths [Å] for $Eu_3Ir_2In_{15}$ at 100(2) K with Estimated Standard Deviations in Parentheses

label	distance	label	distance
Eu(1)−In(3)	3.2022(8)	Ir−In(4)#13	2.8662(3)
Eu(1)−In(5)#4	3.4162(4)	In(1)−In(4)#15	3.1460(5)
Eu(2)−In(2)	3.3025(9)	In(2)−In(4)	3.1457(12)
Eu(2)−In(4)#8	3.4278(8)	In(2)−In(5)	3.2106(9)
Eu(2)−In(5)#12	3.5885(6)	In(2)−In(3)#13	3.2732(6)
Eu(2)−In(1)#10	3.6705(8)	In(3)−In(5)#5	3.1329(8)
Eu(2)−In(3)#13	3.8310(10)	In(3)−In(4)#12	3.1942(8)
Ir−In(1)	2.5775(6)	In(4)−In(5)#21	3.0869(10)
Ir−In(2)#5	2.8048(7)	In(4)−In(4)#13	3.2301(15)
Ir−In(3)	2.6744(8)		

2.5. Computational Details. Density functional theory based first-principles calculations of the ternary compounds $Eu_3Ir_2In_{15}$, $Eu_5Ir_4In_{10}$, and $Ce_5Ir_4Sn_{10}$ have been carried out with a local density approximation (LDA)[21] as implemented in Quantum Espresso code.[22] $Ce_5Ir_4Sn_{10}$ was selected for the structural comparison, and $Eu_5Ir_4In_{10}$ is a hypothetical structure. We employed the augmented-wave method[23] along with consideration of scalar relativistic effects for d-electrons of iridium. Europium and indium have been addressed with norm-conserved[24] pseudopotentials. Plane wave basis was truncated with energy cutoffs of 60 Ry in representation of wave functions, and density cutoff was fixed as 480 Ry. k-Meshes of 5 × 5 × 15 (tetragonal) are used to sample Brillouin zone integration for structural optimization. To compute the chemical potential of the respective elements (Eu, Ir, and In), in particular, Wyckoff position in the crystal, we fix the atomic configuration to maintain the symmetry of the crystal. For the electronic structure calculation, Brillouin zone is sampled by a dense 10 × 10 × 25 k-point mesh. To understand the

structural stability and nature of the chemical bonding in such compounds, we have looked for the nature of the orbital overlap. Total charge density minus superposition of atomic densities has been computed for all three complexes ($Eu_3Ir_2In_{15}$, $Eu_5Ir_4In_{10}$, and $Ce_5Ir_4Sn_{10}$).

2.6. Magnetic Measurements. Magnetic measurements on bulk samples were performed using polycrystalline samples of $Eu_3Ir_2In_{15}$ with a quantum design magnetic property measurement system–superconducting quantum interference device (MPMS-SQUID) dc magnetometer. Temperature-dependent magnetization data were collected in both field-cooled (FC) and zero-field-cooled (ZFC) modes in the temperature range 2 to 300 K at an applied magnetic field of 1000 Oe. Field-dependent magnetization data were collected at 300 and 2 K for $Eu_3Ir_2In_{15}$ with field sweeping from −60 to 60 kOe.

2.7. X-ray Absorption Near-Edge Spectroscopy (XANES). XANES experiments were performed at the Sector 20 bending magnet beamline (PNC/XSD, 20-BM) of the Advanced Photon Source at the Argonne National Laboratory. Measurements at the Eu LIII edge were performed in the transmission mode using gas ionization chambers to monitor the incident and transmitted X-ray intensities. A third ionization chamber was used in conjunction with an Fe foil to provide internal calibration for the alignment of the edge positions. Monochromatic X-rays was obtained using a Si (111) double-crystal monochromator. The monochromator was calibrated by defining the inflection point (first derivative maxima) of Fe foil as 7111 eV. A Rh-coated X-ray mirror was utilized to suppress higher-order harmonics. XANES samples were prepared by mixing an appropriate amount of the finely ground $Eu_3Ir_2In_{15}$ with boron nitride. The mixture was pressed to form a self-supporting pellet, and the measurements were performed at 300 K. Care was taken to suppress distortion in the data from thickness effects.

2.8. Electrical Resistivity. The resistivity measurements were performed on a pellet of $Eu_3Ir_2In_{15}$ in the temperature range 3−300 K using a four-probe dc technique. Four very thin copper wires with a diameter of 50 μm were glued to the pellets using a strongly conducting silver epoxy paste. The measurement was carried out using a quantum design physical property measurement system (QD-PPMS). The measurements were performed applying a low voltage, 0.1 mV, with an applied current of 5 mA.

3. RESULTS AND DISCUSSION

3.1. Reaction Chemistry. The compound was obtained serendipitously during our quest to synthesize a silicide in indium flux. The synthesis strategy has been employed similar to our previous reports, where In was used as active flux.[25−31] We had used silicon beads (0.1 mm) for the synthesis. At the end of the reaction, it was noticed that most of the silicon beads remained unreacted, whereas some silicon beads turned into hollow bowls inside which shiny rod-shaped single crystals were found. Focusing on the point from which the crystals are originated revealed an interesting fact. There are many small crystallites (Figure 1) at the bottom, which we believe are the nucleation centers for the crystal growth. To further understand the role of silicon, we performed a control reaction without using silicon, keeping all other reaction parameters the same as before. The yield of single crystals in this case was much lower (∼60%) in comparison to the previous case (95%), which indirectly supports the fact that silicon acts as a nucleation site. Silicon did not participate in the reaction most probably because of its high melting point and poor diffusibility in the reaction mixture.

3.2. Crystal Structure. $Eu_3Ir_2In_{15}$ crystallizes in the tetragonal crystal structure with the $P4/mbm$ space group in the $Eu_3Co_2In_{15}$ structure type. The lattice parameters are $a = b$ = 14.8186(14) Å and c = 4.3742(4) Å. The prototype was described as a Zintl phase under the Zintl−Klemm formalism. The overall structure can be described as a 3D network of

$[Ir_2In_{15}]$ constructed as one-dimensional (1D) channels of eight- and five-membered rings (Figure 2). The Eu atoms are

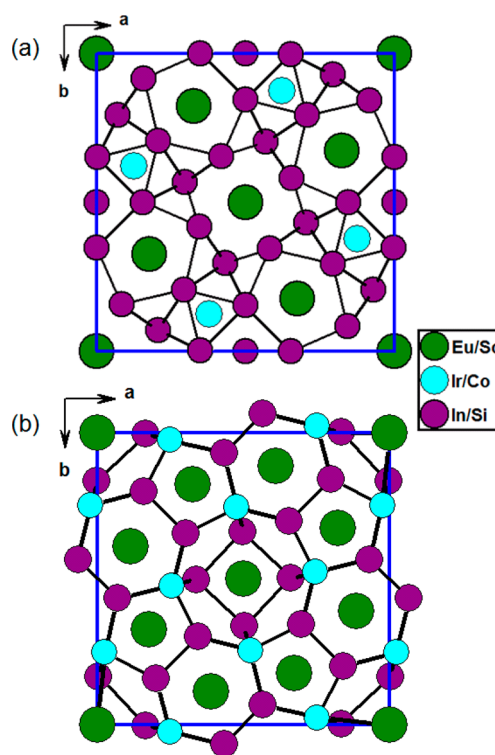**Figure 2.** Crystal structure of (a) $Eu_3Ir_2In_{15}$ and (b) $Sc_5Co_4Si_{10}$ shown along the c-direction. The unit cells are marked with solid blue lines.

embedded inside these 1D channels along the c-direction. The Eu−Eu bond distance along this direction is 4.3901(2) Å. Surprisingly, there is no Eu−Eu bonding along any other direction. This Eu−Eu distance is comparable to that of many other Eu-based compounds such as Eu_2AgGe_3, Eu_2AuGe_3, and $EuAuIn_4$, which also have an exclusively divalent Eu moiety.[10,32]

The structure of $Eu_3Ir_2In_{15}$ can be correlated with another structural prototype, $Sc_5Co_4Si_{10}$, which also crystallizes in the tetragonal $P4/mbm$ space group. In the case of $Eu_3Ir_2In_{15}$, the In atoms construct a 3D cage-like structure that consists of an eight-membered ring at the center surrounded by five-membered rings that are linked by triangular rings. The Eu atoms are embedded in the eight- and five-membered rings, whereas Ir atoms sit inside the triangular rings (Figure 2a). $Sc_5Co_4Si_{10}$ also has a concentric four-membered ring surrounded by an eight-membered ring at its core, which are again surrounded by five- and six-membered rings intercon-nected by bonds with five- and six-membered ring atoms/side sharing, respectively. The transition metal (Co in this case), unlike the first compound, actively participates in the cage formation along with Si, whereas Sc atoms occupy the centers of all the rings. The crystallographic positions in these compounds have been compared in Scheme 1. It can easily be seen that all the local symmetries are the same in both series; the only difference is an extra Wyckoff position at $2c$, which is occupied by an In1 atom, and hence the compound $Eu_3Ir_2In_{15}$ (including $Eu_3Co_2In_{15}$) can be viewed as a vacancy-filled variant of the $Sc_5Co_4Si_{10}$ type. At this point, it is worthwhile to compare the coordination environments of the corresponding crystallographic sites in $Eu_3Ir_2In_{15}$ and $Sc_5Co_4Si_{10}$ as shown Figure 3. Eu1 (wyck. no. $2b$) is surrounded by 12 In atoms and

Scheme 1. Crystallographic Relationship between the Structures $Sc_5Co_4Si_{10}$ and $Eu_3Ir_2In_{15}$

Sc3 (2b)	Sc2 (4h)	Sc1 (4h)		Si3 (4g)	Si1 (8j)	Si2 (8i)	Co (8i)
0.0000	0.2500	0.1756		0.0679	0.1638	0.1575	0.2460
0.0000	0.000	0.6756		0.5679	0.0031	0.1985	0.0240
0.0000	0.8106	0.5000		0.0000	0.5000	0.0000	0.0000

Origin Shift (0, 0, ½)

Eu1 (2b)	Eu2 (4h)	Ir (4h)	In1 (2c)	In2 (4g)	In3 (8j)	In4 (8i)	In5 (8i)
0.0000	0.3248	0.1229	0.0000	0.2065	0.0682	0.1526	0.1568
0.0000	0.1752	0.3770	0.5000	0.2935	0.2052	0.4986	0.0825
0.5000	0.5000	0.5000	0.5000	0.0000	0.5000	0.0000	0.0000

2 Eu atoms, whereas Sc3 (wyck. no. 2b) is surrounded by 12 Si atoms, four Co atoms, and two Sc atoms. Eu2 (wyck. no. 4h) is surrounded by eight In atoms. Sc2 on the contrary is surrounded by 10 Si and four Co atoms. Ir is in a tricapped bipyramidal structure consisting of nine In atoms, whereas Sc1 is in a 12-membered pseudo-Frank−Kasper cage. The In atoms have the following coordination geometries: In1, bicapped tetragonal bipyramid; In2, distorted bicapped tetragonal bipyramid; In3, capped tetragonal bipyramid; In4, distorted

bicapped tetragonal bipyramid; In5, distorted trigonal bipyramid. In $Sc_5Co_4Si_{10}$, the three Si atoms reside in a tetracapped trigonal bipyramid and pseudo-Frank−Kasper and tricapped trigonal bypyramids. The minimum Eu−Eu bond distance in $Eu_3Ir_2In_{15}$ is 4.3901(2) Å, which is typical in compounds with Eu, as we observed in Eu_2AuGe_3, Eu_2AgGe_3, and $EuIrIn_4$.[32−34] This was further confirmed by temperature-dependent magnetic susceptibility measurement on the sample, which clearly indicated that the majority of Eu exists in the divalent state (∼88%). In the case of the $RE_5T_4X_{10}$ series, all the compounds reported so far contain the rare earth atoms in a trivalent state.[17,35,36] Our literature survey on these two classes of compounds reveals an astonishing fact: all the compounds belonging to the $RE_5T_4X_{10}$ series contain group 14 elements as the p-block constituent, whereas both $Eu_3Co_2In_{15}$ reported previously by Lei et al.[12] and the current compounds have group 13 elements (indium in this case) as the p-block constituent. In order to verify this hypothesis, we taken a few controls to synthesis $Eu_3Ir_2In_{15}$ and $Eu_5Ir_4In_{10}$ by the direct method. This was done by heating stoichiometric elements in an evacuated quartz tube, heating to 1000 °C in 10 h, annealing at 850 °C for 48 h, and cooling to room temperature (30 °C) in 48 h. Indeed, we found that although the first compound formed, the second compound did not form. To further support our experimental observations, we performed basic electronic structure calculations regarding the stability of each crystallographic position in these two types in a given coordination environment, which, on the whole, will dictate the stability of the compound itself as discussed in the following section.
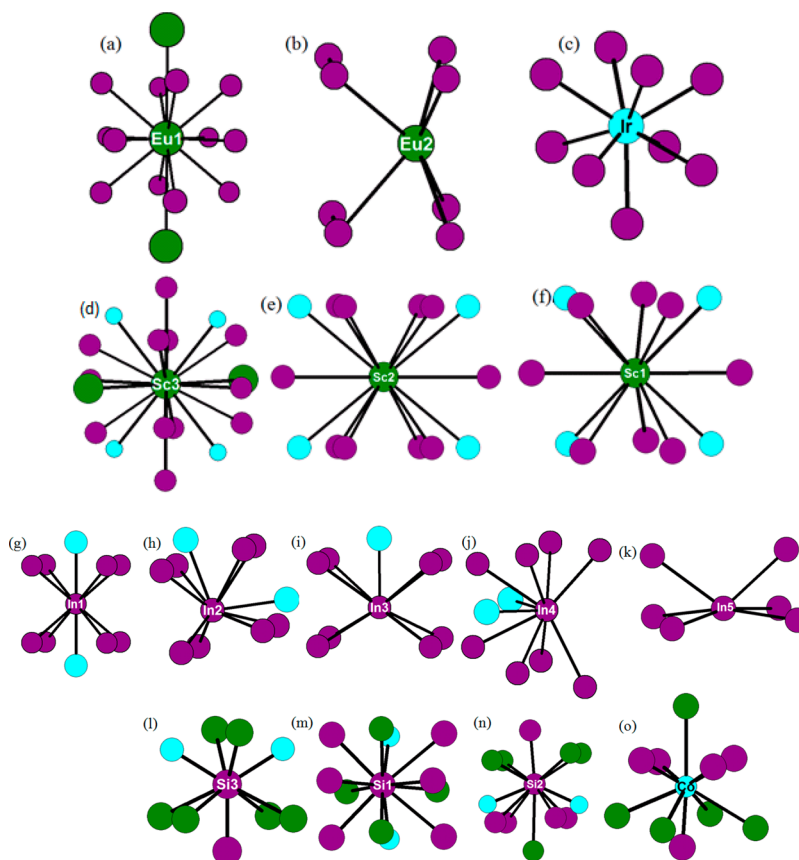

Figure 3. Comparison of coordination environments of all the crystallographic sites in $Eu_3Ir_2In_{15}$ and $Sc_5Co_4Si_{15}$.

3.2. Relative Thermodynamic Stability: A First-Principles Study. The question of the preference of the 3:2:15 stoichiometric ratio for Eu, Ir, and In in the Eu−Ir−In ternary series has been addressed through first-principles study based on density functional theory (DFT). To get insight into the thermodynamic feasibility, a thorough scrutiny of the local chemical potential of the atoms in different crystallographic sites has been carried out. In this context, we considered $Ce_5Ir_4Sn_{10}$ (RE = Ce, T = Ir, X = Sn) and $Eu_3Ir_2In_{15}$, which are in different stoichiometric ratios (5:4:10 vs 3:2:15) but existing with the same crystal symmetry. A hypothetical model compound, $Eu_5Ir_4In_{10}$, has also been considered in this respect. The structures of both $Eu_3Ir_2In_{15}$ and $Eu_5Ir_4In_{10}$ were optimized for the most stable geometry, as shown in Figure 4.
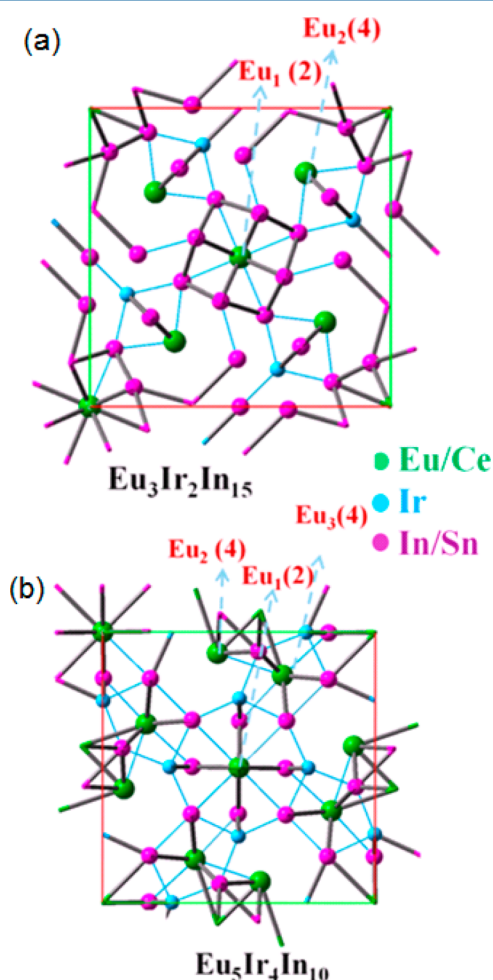
Figure 4. Optimized geometries of the ternary compounds $Eu_3Ir_2In_{15}$ (a) and $Eu_5Ir_4In_{10}$ (b). Green circles denote the europium atoms and corresponding Wyckoff positions in the lattice. Cyan and pink colors represent iridium and indium atoms and their crystallographic positions.

The computational findings (Figure S3) excellently corroborate with the experimental[6] bulk cohesive energy (E_M) for respective elements (Eu, Ir, and In) and lattice constants for $Eu_3Ir_2In_{15}$ and $Ce_5Ir_4Sn_{10}$. Bulk cohesive energy ($E_{Cohesive}$) of the element M is defined as follows:

$$E_{Cohesive} = [E_{Bulk} - (n_{Bulk}E(M))]/n_{Bulk} \qquad (1)$$

where E_{Bulk} is the free energy of the most stable elemental form of any metal (M = Eu, Ir, In, Ce, Sn) in their bulk crystalline state. n_{Bulk} corresponds to the number of atoms in the bulk unit cell, and $E(M)$ = free energy of an isolated M atom.

In fact, iridium possesses the highest bulk cohesive energy (6.94 eV/atom) among all constituent elements (for Eu and In 1.86 and 2.52 eV/atom, respectively). Thus, melting of iridium from its bulk state to the compound is expected to be the rate-determining step for the formation of Eu−Ir−In ternary compounds.

The chemical potential, $\mu_{site}(M)$, of the species M for its occupancy in a particular site (Wyckoff position) represents its thermodynamic stability and is expressed as

$$\mu_{Site}(M) = E_{Compound} - E_{Compound-M} - E_M \qquad (2)$$

where $E_{Compound}$ is the total free energy of the ternary compound, $E_{Compound-M}$ is the free energy of compound when M is missing from one particular site, and $E_M = E_{Bulk}/n_{Bulk}$. Indeed, the chemical potential corresponds to the stability of different Wyckoff positions occupied by the respective elements (eq 2). All spatially variant values of the chemical potentials were carefully accounted for, and these were related to the growth of the compounds. Interestingly, it was found that μ^{37} is the lowest among all other values (Table 5), and Ir becomes stable only for the cases of $Eu_3Ir_2In_{15}$ and $Ce_5Ir_4Sn_{10}$. On the other hand, μ^{37} becomes positive (+0.09 eV) for $Eu_5Ir_4In_{10}$, dictating the thermodynamic infeasibility of the melting of Ir from its bulk state to form a compound of 5:4:10 composition. This process can be attained only by applying a perturbing influence such as an extremely high temperature or catalyst. A close look into the structure of $Eu_5Ir_4In_{10}$ revealed that there are two intrinsic vacancies in two Wyckoff positions for $Eu_5Ir_4In_{10}$ per formula unit compared to the $Eu_3Ir_2In_{15}$ analogue. Constituent atoms in $Eu_5Ir_4In_{10}$ are rearranged in such a way that there is an increase in the number of Ir atoms per formula unit at the cost of a decrease in In atoms compared to $Eu_3Ir_2In_{15}$. We find that there are five In atoms in the first coordination zone of Ir atoms for both $Eu_3Ir_2In_{15}$ and $Eu_5Ir_4In_{10}$, whereas there are four extra In atoms as neighbors in the secondary coordination zone (after consideration of the cutoff distance as 3 Å) only for $Eu_3Ir_2In_{15}$. Thus, there is a reduction of the effective coordination number of Ir in $Eu_5Ir_4In_{10}$ composition, consequently reducing its stability in the lattice environment of $Eu_5Ir_4In_{10}$. On the other hand, Eu as well as In sites are found to be very stable with negative chemical potential values (Table 5) for both possible compositions ($Eu_3Ir_2In_{15}$ and $Eu_5Ir_4In_{10}$). In order to understand the bonding feature, the strength of the chemical bonding was determined in terms of the net orbital overlap after the formation of compounds (Figure 5). In the case of $Eu_3Ir_2In_{15}$, it was found that the bonding feature is extended throughout the solid and there is a significant overlap among all the elements in $Eu_3Ir_2In_{15}$, which is also observed in the case of $Ce_5Ir_4Sn_{10}$. But the overlap picture is completely different in the case of $Eu_5Ir_4In_{10}$ (Figures 5 and 6) due to the predominance of localized bonding surrounding Eu. This does not stabilize the whole structural framework in this compound. Hence, it is confirmed that the delocalized overlap picture involving all the elements in the compound determines its stability, preferring a particular composition.

We have also looked at the quantitative evaluation of chemical pressure and compared the possibility of different stoichiometries at various thermodynamic conditions. From the

Table 5. Chemical Potential Values (μ_{site}(M), in eV) with Weight Factor (Degeneracy) Corresponding to the Different Occupied Wyckoff Positions Given in Parentheses

compound	μ_{site}(Eu/Ce)	μ_{site} [37]	μ_{site}(In)/Sn	atomic sites
$Eu_3Ir_2In_{15}$	−5.38 (2)	−0.37(4)	−1.39 (8)	24
	−4.46 (4)		−0.95 (8)	37
			−2.30 (4)	18
			−1.49 (6)	4
			−2.20 (4)	31
$Eu_5Ir_4In_{10}$	−5.72 (2)	0.09 (8)	−3.41 (8)	11
	−5.77 (4)		−3.17 (8)	18
	−5.38 (4)		−4.01 (4)	37
$Ce_5Ir_4Sn_{10}$	−3.11 to −4.01 (10)	−4.09 (8)	(∼) −3.54 (20)	
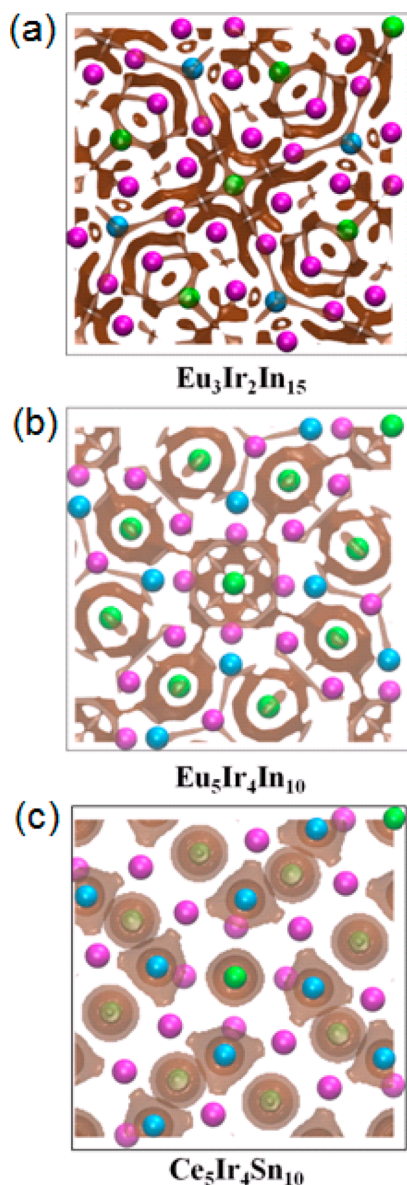
Figure 5. Charge density isosurfaces for the top view of (a) $Eu_3Ir_2In_{15}$, (b) $Eu_5Ir_4In_{10}$, and (c) $Ce_5Ir_4Sn_{10}$. The integrals of the total charge density minus superposition of atomic densities have been plotted, and brown isosurfaces show the regions of net charge density due to the orbital overlap. Green, cyan, magenta, pale green, and violet spheres represent Eu, Ir, In, Ce, and Sn atoms, respectively. The isosurfaces shown correspond to (a, b) 0.2 e/Å³ and (c) 0.1 e/Å³.
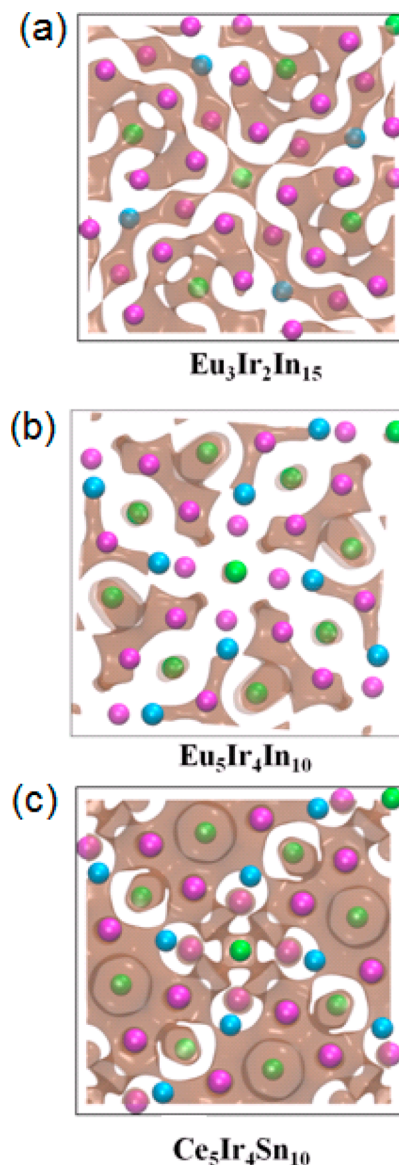
Figure 6. Charge density isosurfaces for the top view of (a) $Eu_3Ir_2In_{15}$, (b) $Eu_5Ir_4In_{10}$, and (c) $Ce_5Ir_4Sn_{10}$. Total charge densities have been plotted, and brown isosurfaces show the regions of total charge density in the compounds. The isosurfaces shown correspond to (a, b) 0.02 e/Å³.

detailed structural analysis, we found that, for $Eu_3Ir_2In_{15}$, $a/c = b/c = 3.50$ (volume = 834.40 Å³/f.u.); for $Eu_5Ir_4In_{10}$, $a/c = b/c = 3.15$ (volume = 757.08 Å³/f.u.); and for $Ce_5Ir_4Sn_{10}$, $a/c =$

3.03 (volume = 860.95). Volume shrinkage of 6.47% results in the volume of $Eu_5Ir_4In_{10}$, which amounts to 41.21 GPa as internal pressure per formula unit of $Eu_3Ir_2In_{15}$. Thus, $Eu_3Ir_2In_{15}$ is entropically more favorable with respect to the other possibility ($Eu_5Ir_4In_{10}$). Moreover, the exchange functional captures the qualitative trend from the antiferromagnetic order in $Eu_3Ir_2In_{15}$, which is corroborative with our experimental findings. Thus, magnetic coupling is accompanied by a majority of +2 valence states of Eu in $Eu_3Ir_2In_{15}$, which further stabilizes the system.

3.3. Magnetic Properties. The temperature-dependent molar magnetic susceptibility of a polycrystalline sample of $Eu_3Ir_2In_{15}$ at an applied field of 1 kOe is shown in Figure 7a.
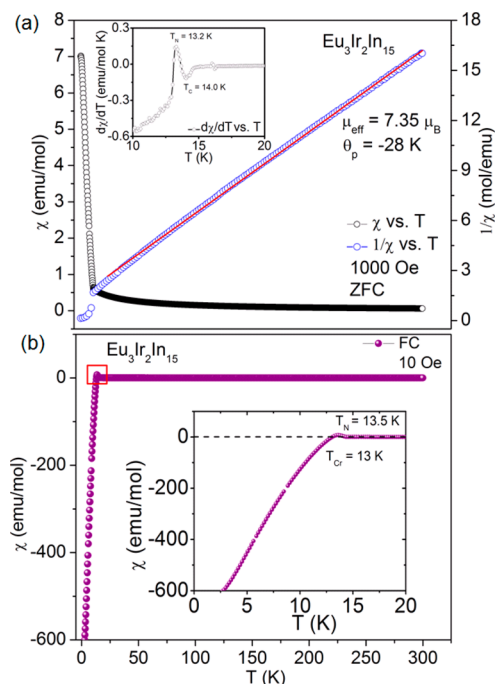

Figure 7. (a) Temperature dependence of molar magnetic susceptibility (χ) and inverse magnetic susceptibility of $Eu_3Ir_2In_{15}$ at an applied magnetic field of 1000 Oe. The inset shows temperature dependence of the first-order derivative of χ. (b) Temperature dependence of molar magnetic susceptibility (χ) at a low magnetic field of 10 Oe. Inset shows a zoomed portion of the demagnetization.

The magnetic susceptibility of the sample remains almost unchanged with decreasing temperature down to 50 K, and then it slowly starts to increase. A steep increase in the magnetic susceptibility is observed below 15 K (T_c), which may correspond to a ferromagnetic ordering among the Eu spins. Another transition is observed below 13.2 K (T_N), leading to a ferromagnetic to antiferromagnetic transition. This kind of ferromagnetic to antiferromagnetic transition has previously been observed in case of $Ce(Fe_{1-x}Co_x)_2$.[38] The inverse susceptibility curve obeys the Curie–Weiss law, $\chi = C/(T - \theta_p)$ above 20 K and then deviates from linearity below this temperature. A linear fit with the Curie–Weiss law in the temperature range 20–300 K gives the value of the paramagnetic Curie temperature (θ_p) of −28 K and an effective magnetic moment (μ_{eff}) of 7.35 μ_B/Eu ion. The negative sign of θ_p indicates an overall antiferromagnetic interaction between the adjacent Eu centers. The calculated effective magnetic moment/Eu is slightly less than the spin-only value for a

divalent Eu (7.94 μ_B), which hints toward mix valency at Eu positions. At a lower magnetic field (10 Oe), the magnetic susceptibility decreases sharply with decreasing temperature below 13 K and becomes negative, indicating a possible demagnetized state at low temperature (Figure 7b). Although this phenomenon was observed previously in Yb-based intermetallic compounds, such as $YbMn_{0.17}Si_{1.88}$[39] and $YbFe_4Al_8$[40] and other oxide-based materials, it has, to the best of our knowledge, never been encountered in any Eu-based intermetallic compound. The demagnetization was explained considering a spontaneous ferromagnetic moment (M_T) at the magnetic ordering temperature, due to the canting of transition metal spins, whereas the rare earth moment is coupled antiparallel to the effective transition metal moment (M_T) as well as to the external applied magnetic field. As the critical temperature is reached, the rare earth moment dominates over the transition metal moment and the system shows a negative magnetization. This model, however, cannot be applied to $Eu_3Ir_2In_{15}$, because there is no magnetic spins arising from iridium, and hence there is no question of canted iridium spins. As a result, this issue urges a deeper investigation into the $5d$ states of Ir toward the overall magnetic properties of this compound and will be addressed in our future work.

In order to have a greater insight into the magnetic properties of this compound, we performed field-dependent magnetization at 2 and 300 K (Figure 8). At high temperature,
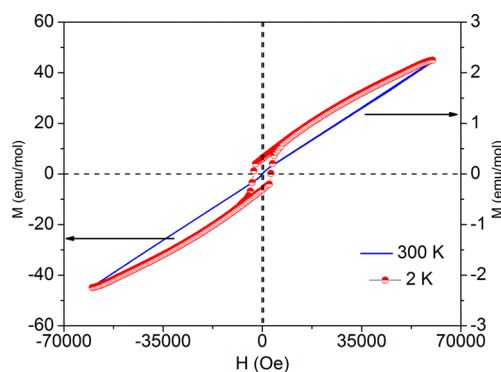

Figure 8. Field dependence of molar magnetization of $Eu_3Ir_2In_{15}$ at 2 (red) and 300 K (blue), respectively, in the range of −60 to +60 kOe.

i.e., 300 K, magnetization increased linearly with increasing magnetic field, indicating simple paramagnetic behavior. At low temperature, 2 K, however, a strong hysteresis is observed up to 7 kOe, beyond which the magnetic moment increases almost linearly up to the maximum applied magnetic field, 60 kOe. The switching from a ferromagnetic to antiferromagnetic state upon increasing the magnetic field can be explained based on the spin flip mechanism,[41] wherein the magnetic spins reverse their direction.

To unambiguously confirm the valency of Eu, we performed an XANES study on crushed single crystals of $Eu_3Ir_2In_{15}$, and we found a sharp peak at 6973 eV along with a broad hump at 6982 eV, which can be assigned to di- and trivalent europium, respectively (Figure 9).[33,42] Integration over the respective areas yielded a ratio of almost 88% of Eu in divalent state and the rest of it (12%) in trivalent state. This result is in good agreement with the magnetic susceptibility data.

3.4. Resistivity. The temperature-dependent resistivity data for $Eu_3Ir_2In_{15}$ are shown in Figure 10. Resistivity increases almost linearly with increasing temperature. The slight

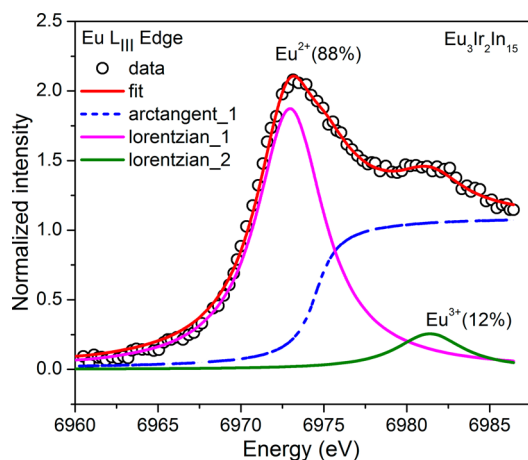**Figure 9.** Eu LIII-edge X-ray absorption study on crushed single crystals of $Eu_3Ir_2In_{15}$ and fitted with a Lorentzian equation to calculate the Eu^{2+} to Eu^{3+} ratio.
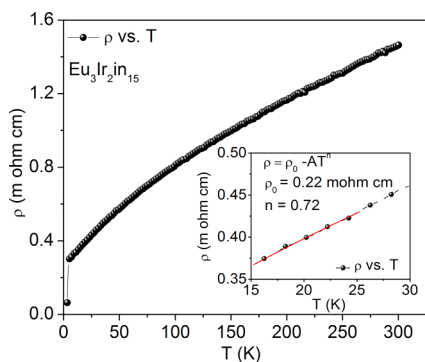

Figure 10. Temperature dependence of electrical resistivity of $Eu_3Ir_2In_{15}$ in the temperature range 3−300 K. Inset shows fitting with the power law $\rho = \rho_0 - AT^n$ in the low-temperature range.

curvature may arise due to the crystal field effect in the system. Surprisingly, no magnetic ordering was observed in the resistivity data. The sudden decrease in the resistivity at around 3.4 K is due to a superconducting transition in small quantity of indium, which was inevitably present in the sample. To understand the nature of the ground state of the system, the curve was fitted with a power law, $\rho = \rho_0 - At^n$, just above ferromagnetic transition (14−20 K),[43] where ρ_0 is residual resistivity and n is the power, which were calculated to be 0.22 mΩcm and 0.72, respectively. The value of n is less than 1, which indicates that the compound resides in a non-Fermi liquid ground state in the vicinity of the magnetic transition. A similar observation was reported for $URu_{2-x}Re_xSi_2$.[44]

4. CONCLUSION

We used a metal flux technique to synthesize a new compound, $Eu_3Ir_2In_{15}$, which is the second member in the $Eu_3Co_2In_{15}$ family. The crystal structure, magnetic, and transport properties were studied in detail. It was further shown how silicon plays a crucial role not only in facilitating high-quality crystal growth but also with higher yield. We correlated the structure of $Eu_3Ir_2In_{15}$ with $Sc_5Co_4Si_{10}$ and rationalized the formation and relative stabilities of $Eu_3Ir_2In_{15}$ in comparison with a hypothetical compound, $Eu_5Ir_4In_{10}$, conceived from the already reported $Ce_5Ir_4Sn_{10}$ structure. Our computations established that the former is thermodynamically more stable than the

latter based on the fact that, in a given coordination environment, Ir crystallographic sites have lower chemical potential in the case of $Eu_3Ir_2In_{15}$ over $Eu_5Ir_4In_{10}$. We also observed an anomalous demagnetization of $Eu_3Ir_2In_{15}$ at lower applied magnetic fields below 14 K, which is distinctively different from those previously reported in the case of $YbFe_4Al_8$ and $YbMn_{0.8}Si_{1.2}$ and needs further experimental verification, which will be addressed in the future. Hence it can be concluded that $Eu_3Ir_2In_{15}$ and related compounds with similar structural type need further experimental and theoretical endeavors to understand the interplay of stoichiometric features and consequential properties.

■ ASSOCIATED CONTENT

Ⓢ Supporting Information

The Supporting Information is available free of charge on the ACS Publications website at DOI: 10.1021/acs.inorg-chem.5b01926.

Additional figures (PDF)

Crystallographic data (CIF)

■ AUTHOR INFORMATION

Corresponding Author

*Phone: 080-22082298. Fax: 080-22082627. E-mail: sebastiancp@jncasr.ac.in (S. C. Peter).

Notes

The authors declare no competing financial interest.

■ ACKNOWLEDGMENTS

■ REFERENCES

(1) Deakin, L.; Lam, R.; Marsiglio, F.; Mar, A. *J. Alloys Compd.* **2002**, *338*, 69−72.

(2) Kauzlarich, S. M.; Brown, S. R.; Jeffrey Snyder, G. *Dalton Trans.* **2007**, 2099−2107.

(3) Brown, S. R.; Kauzlarich, S. M.; Gascoin, F.; Snyder, G. J. *Chem. Mater.* **2006**, *18*, 1873−1877.

(4) Cox, C. A.; Toberer, E. S.; Levchenko, A. A.; Brown, S. R.; Snyder, G. J.; Navrotsky, A.; Kauzlarich, S. M. *Chem. Mater.* **2009**, *21*, 1354−1360.

(5) Toberer, E. S.; Cox, C. A.; Brown, S. R.; Ikeda, T.; May, A. F.; Kauzlarich, S. M.; Snyder, G. J. *Adv. Funct. Mater.* **2008**, *18*, 2795−2800.

(6) Toberer, E. S.; Brown, S. R.; Ikeda, T.; Kauzlarich, S. M.; Jeffrey Snyder, G. *Appl. Phys. Lett.* **2008**, *93*, 062110.

(7) Rauscher, J. F.; Cox, C. A.; Yi, T.; Beavers, C. M.; Klavins, P.; Toberer, E. S.; Snyder, G. J.; Kauzlarich, S. M. *Dalton Trans.* **2010**, *39*, 1055−1062.

(8) Sun, Y.; Chen, X.-Q.; Franchini, C.; Li, D.; Yunoki, S.; Li, Y.; Fang, Z. *Phys. Rev. B: Condens. Matter Mater. Phys.* **2011**, *84*, 165127.

(9) Tsujii, N.; Uvarov, C. A.; Klavins, P.; Yi, T.; Kauzlarich, S. M. *Inorg. Chem.* **2012**, *51*, 2860−2866.

(10) Sarkar, S.; Gutmann, M. J.; Peter, S. C. *Cryst. Growth Des.* **2013**, *13*, 4285−4294.

(11) Hoffmann, R. D.; Pottgen, R. *Z. Kristallogr. - Cryst. Mater.* **2001**, *216*, 127−145.

(12) Lei, X.-W.; Zhong, G.-H.; Li, L.-H.; Hu, C.-L.; Li, M.-J.; Mao, J.-G. *Inorg. Chem.* **2009**, *48*, 2526−2533.

(13) Kalychak, Y. M.; Zaremba, V. I.; Pottgen, R.; Lukachuk, M.; Hoffmann, R.-D. *Handbook on the Physics and Chemistry of Rare Earths*; Elsevier B. V., 2005; Vol. *34*.

(14) Kolenda, M.; Hofmann, M.; Leciejewicz, J.; Penc, B.; Szytuła, A. *Appl. Phys. A: Mater. Sci. Process.* **2002**, *74*, s769−s771.

(15) Patil, N. G.; Ramakrishnan, S. *Phys. B* **1997**, *237−238*, 594−596.

(16) Subbarao, U.; Sarkar, S.; Gudelli, V. K.; Kanchana, V.; Vaitheeswaran, G.; Peter, S. C. *Inorg. Chem.* **2013**, *52*, 13631−13638.

(17) Peter, S. C.; Rayaprol, S.; Francisco, M. C.; Kanatzidis, M. G. *Eur. J. Inorg. Chem.* **2011**, *2011*, 3963−3968.

(18) *SAINT*, 6.02 ed.; Bruker AXS Inc.: Madison, WI, USA, 2000.

(19) Sheldrick, G. M. *SHELXS 97*; University of Göttingen: Göttingen, Germany, 1997.

(20) Sheldrick, G. M. *SHELXTL, Structure Determination Program*, version 5 ed.; Siemens Analytical X-ray Instruments Inc.: Madison, WI, 1995.

(21) Becke, A. D. *Phys. Rev. A: At., Mol., Opt. Phys.* **1988**, *38*, 3098.

(22) Giannozzi, P.; Baroni, S.; Bonini, N.; Calandra, M.; Car, R.; Cavazzoni, C.; Ceresoli, D.; Chiarotti, G. L.; Cococcioni, M.; Dabo, I. *J. Phys.: Condens. Matter* **2009**, *21*, 395502.

(23) Blöchl, P. E. *Phys. Rev. B: Condens. Matter Mater. Phys.* **1994**, *50*, 17953.

(24) Bachelet, G. B.; Schläter, M. *Phys. Rev. B: Condens. Matter Mater. Phys.* **1982**, *25*, 2103.

(25) Subbarao, U.; Sebastian, A.; Rayaprol, S.; Yadav, C. S.; Svane, A.; Vaitheeswaran, G.; Peter, S. C. *Cryst. Growth Des.* **2013**, *13*, 352−359.

(26) Subbarao, U.; Peter, S. C. *J. Chem. Sci.* **2013**, *125*, 1315−1323.

(27) Subbarao, U.; Peter, S. C. *Inorg. Chem.* **2012**, *51*, 6326−6332.

(28) Sebastian, C. P.; Salvador, J.; Martin, J. B.; Kanatzidis, M. G. *Inorg. Chem.* **2010**, *49*, 10468−10474.

(29) Chondroudi, M.; Peter, S. C.; Malliakas, C. D.; Balasubramanian, M.; Li, Q. A.; Kanatzidis, M. G. *Inorg. Chem.* **2011**, *50*, 1184−1193.

(30) Subbarao, U.; Jana, R.; Chondroudi, M.; Balasubramanian, M.; Kanatzidis, M. G.; Peter, S. C. *Dalton Trans.* **2015**, *44*, 5797−5804.

(31) Subbarao, U.; Sarkar, S.; Peter, S. C. *J. Solid State Chem.* **2015**, *226*, 126−132.

(32) Sebastian, C. P.; Malliakas, C. D.; Chondroudi, M.; Schellenberg, I.; Rayaprol, S.; Hoffmann, R.-D.; Pöttgen, R.; Kanatzidis, M. G. *Inorg. Chem.* **2010**, *49*, 9574−9580.

(33) Sarkar, S.; Peter, S. C. *Inorg. Chem.* **2013**, *52*, 9741−9748.

(34) Sarkar, S.; Gutmann, M. J.; Peter, S. C. *Dalton Trans.* **2014**, *43*, 15879−15886.

(35) Galli, F.; Feyerherm, R.; Hendrikx, R. W. A.; Dudzik, E.; Nieuwenhuys, G. J.; Ramakrishnan, S.; Brown, S. D.; Smaalen, S. v.; Mydosh, J. A. *J. Phys.: Condens. Matter* **2002**, *14*, 5067.

(36) Patil, N. G.; Ramakrishnan, S. *Phys. Rev. B: Condens. Matter Mater. Phys.* **1997**, *56*, 3360−3371.

(37) Hiraoka, T.; Kinoshita, E.; Tanaka, H.; Takabatake, T.; Fujii, H. *J. Magn. Magn. Mater.* **1996**, *153*, 124.

(38) Zhang, X.; Ali, N. *J. Alloys Compd.* **1994**, *207−208*, 300−303.

(39) Peter, S. C.; Malliakas, C. D.; Kanatzidis, M. G. *Inorg. Chem.* **2013**, *52*, 4909−4915.

(40) Andrzejewski, B.; Kowalczyk, A.; Frąckowiak, J. E.; Toliński, T.; Szlaferek, A.; Pal, S.; Simon, C. *Phys. Status Solidi B* **2006**, *243*, 295−298.

(41) Kishore, S.; Markandeyulu, G.; Rama Rao, K. V. S. *Solid State Commun.* **1998**, *108*, 313−318.

(42) Sarkar, S.; Subbarao, U.; Joseph, B.; Peter, S. C. *J. Solid State Chem.* **2015**, *225*, 181−186.

(43) Kambe, S.; Suderow, H.; Fukuhara, T.; Flouquet, J.; Takimoto, T. *J. Low Temp. Phys.* **1999**, *117*, 101−112.

(44) Maple, M. B.; Butch, N. P.; Bauer, E. D.; Zapf, V. S.; Ho, P. C.; Wilson, S. D.; Dai, P.; Adroja, D. T.; Lee, S. H.; Chung, J. H.; Lynn, J. W. *Physica B* **2006**, *378−380*, 911−914.